

1 **Effect of scour on the fatigue life of offshore wind turbines and**
2 **its prevention through passive structural control**

3

4 Yu Cao¹, Ningyu Wu², Jigang Yang², Chao Chen^{1,3*}, Ronghua Zhu^{3,4*}, Xugang Hua¹,

5

6 ¹Key Laboratory for Bridge and Wind Engineering of Hunan Province, College of Civil
7 Engineering, Hunan University, Changsha, China

8 ²Hebei Construction Investment Offshore Wind Power Co., Ltd., Tangshan, China

9 ³Yangjiang Offshore Wind Laboratory, Yangjiang, China

10 ⁴Ocean College, Zhejiang University, Hangzhou, China

11

12

13

14

15

*Corresponding author: steinchen@hnu.edu.cn, zhu.richard@zju.edu.cn

16 **Abstract**

17 Offshore wind turbine (OWT) support structures are exposed to the risk of fatigue
18 damage and scour, and this risk can be effectively mitigated by installing structural
19 control devices such as tuned mass dampers (TMDs). However, time-varying scour al-
20 tering OWTs' dynamic characteristics has an impact on the TMD design and fatigue
21 life, which was rarely studied before. In this paper, a simplified modal model is used to
22 investigate the influence of scour and a TMD on the fatigue life evaluation of a 5 MW
23 OWT's support structure, and a traditional method and a newly developed optimization
24 technique are both presented to obtain TMD parameters. This optimization technique
25 aims at finding optimal parameters of the TMD which maximizes the fatigue life of a
26 hotspot at the mudline, and effect of time-varying scour can be considered. This study
27 assumes the TMD operates in the FA direction, and the vibration in the SS direction is
28 uncontrolled. Results show that scour can decrease the fatigue life by about 24.1%, and
29 the TMD can effectively suppress vibration and increase the fatigue life. When the
30 scour depth reaches 1.3 times the pile diameter, the TMD with a mass ratio of 1% can
31 increase the fatigue life of OWT's support structure by about 64.6%. Further, it is found
32 that the fatigue life can be extended by 25% with the TMD optimized by the proposed
33 optimization technique, compared to that with the traditionally optimized TMD which
34 does not take the change of dynamic characteristics into account.

35 **Keywords:** scour, offshore wind turbine, structural control, modal analysis, fatigue life.

36

37 **1 Introduction**

38 With the continuous development of large-size fixed-bottom OWTs, local scour
39 and scour protection of pile foundation have become a common issue (L. Wang et al.,
40 2020; X. Wang et al., 2019; F. Zhang et al., 2022). Scour have a significant impact on
41 dynamic characteristics, vibration magnitudes, and thus fatigue life of OWTs under
42 wind and wave loads. On the one hand, the action of currents and waves causes local
43 scour pits around pile foundations, which reduces the burial depth of pile foundations.
44 This phenomenon usually causes a reduction in natural frequencies of OWTs and
45 changes in other dynamic characteristics, possibly leading to resonance, large ampli-
46 tude stress cycles and fatigue damage when one of natural frequencies is close to the
47 rotational frequency of the blades (Sørensen and Ibsen, 2013). On the other hand,

48 current scour protection measures cannot completely avoid scour and have their own
49 shortcomings. For example, armouring protection has the disadvantages that the pro-
50 jectile cannot be accurately cast in complex sea conditions and is easy to be washed
51 away (G. Wang et al., 2023; F. Zhang et al., 2023). Flow-altering protection has the
52 disadvantages of high cost and changing the dynamic characteristics of the foundation
53 (Tang et al., 2023). As offshore structures, wind turbines are vulnerable to corrosion
54 from seawater, which makes the fatigue problem worse (Amirafshari et al., 2021). Thus,
55 the scour-induced changes in dynamic characteristics and risk in resonance inevitably
56 induce a further increase in fatigue damage and deserve in-depth research (Mayall et
57 al., 2018).

58 Many researchers have studied the effect of scour on fatigue damage accumulation
59 in OWTs. For instance, Tempel et al. (2006) investigated the frequency and fatigue of
60 piles under different scour depths and concluded that scour has a little effect on the
61 natural frequencies but a great effect on fatigue damage. Zhang et al. (2021) found that
62 scour depth has a significant influence on monopile impedance. Rezaei et al. (2018)
63 showed that scour leads to an increase in the maximum bending moment of the mono-
64 pile and a shortening of the fatigue life. To mitigate the fatigue damage in OWTs, in-
65 stallng structural control devices is an effective way. It was demonstrated that TMDs
66 have a positive effect on reducing vibration amplitudes of wind turbine systems (Lack-
67 ner and Rotea, 2011a; Dinh and Basu, 2015; Lu et al., 2023; Aydin et al., 2023). Dai et
68 al. (2021) conducted a shaker experiment using a scaled wind turbine model and
69 showed that the installed TMD can suppress the vibration of the structure more effec-
70 tively considering soil-structure interaction (SSI).

71 In the previously mentioned studies, researchers have individually investigated the
72 effect of scour on structural vibration and fatigue, and the structural control by TMDs
73 for OWTs. However, in practice, the effect of scour combining structural control via
74 TMDs could have a significant impact on OWTs' fatigue life. Moreover, whether con-
75 sidering scour could influence the design of TMDs, and TMDs with different parame-
76 ters can also have an impact on fatigue damage accumulation.

77 The purpose of this study is to explore the effect of scour on the fatigue life of
78 wind turbine structures and the control effect of TMD on the fatigue life of wind turbine
79 structures under scour conditions. The authors use a 5 MW single-pile wind turbine as
80 a case study to carry out related research. In this study, ABAQUS is used to establish a

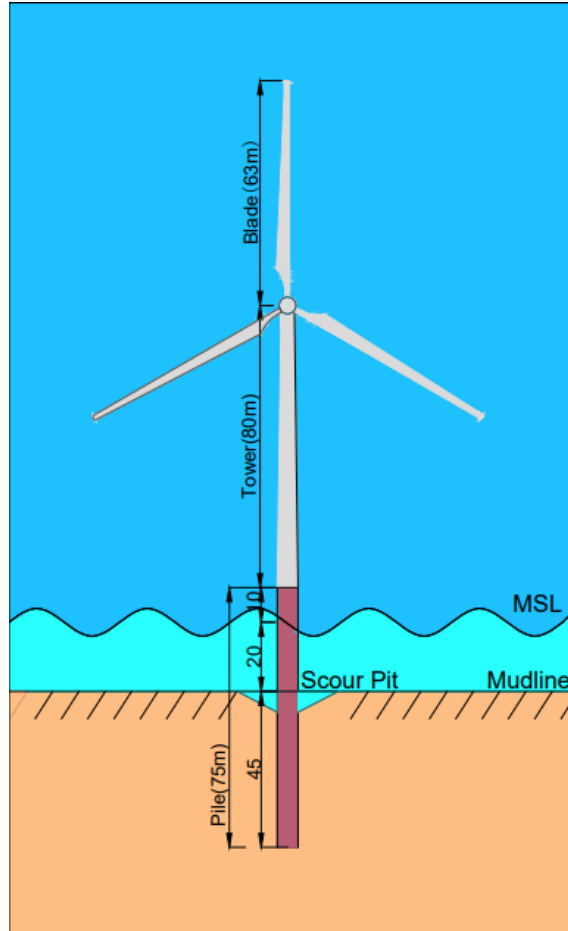
81 detailed SSI model with different scour depths. A finite element model considering
82 wind loads and TMD was established in MATLAB, and the scour effect is considered
83 by establishing a relationship with the ABAQUS model by means of the equivalent
84 stiffness matrix. And the finite element model is simplified to a modal model for fast
85 prediction of fatigue life. The TMD operates in the FA direction and does not work in
86 the SS direction. This study investigates the effect of different scour depths on the per-
87 formance of the TMD and the fatigue life of a 5 MW OWT's support structure including
88 a tower and a monopile foundation, and the optimization of the TMD's parameters con-
89 sidering time-varying scour depths to maximum fatigue life is also presented. This
90 study provides some knowledge of the effects of the time varying scour and the TMD
91 on the fatigue life of wind turbines, as well as a new TMD design method targeting at
92 enhancing fatigue resistance. The rest of the paper is organized as follows: Section 2
93 introduces the numerical models used in the research. Section 3 introduces the tradi-
94 tional TMD design method and the newly developed parameter optimization method.
95 Section 4 describes the load cases for the fatigue analysis, the analysis results of this
96 study and the TMD parameter optimization results. Section 5 concludes the study.

97 **2 Model description**

98 **2.1 Finite element model and implementation of tuned mass damper**

99 An FE model of a monopile-supported OWT installed with a TMD is established
100 in MATLAB. This model contains a flexible tower, a rotor-nacelle assembly (RNA),
101 and an external TMD, considering the foundation flexibility. The model is based on the
102 widely used NREL 5MW reference OWT, and its detailed properties are shown in Ta-
103 ble 1. Three-dimensional beam elements are used to create the FE model and the theo-
104 retical basis is the standard Euler-Bernoulli beam theory. The wind turbine tower is
105 divided into 18 beam elements, and the monopile between the mudline and the mean
106 sea level (MSL) are divided into 4 beam elements. A convergence test by comparing
107 the first natural frequencies shows that 22 beam elements are sufficient. Each element
108 node has 6 degrees of freedom (DOFs) corresponding to the translational and rotational
109 motions in different directions. The mass matrix and stiffness matrix in the equation of
110 motion of the OWT structure can be obtained given the material properties. The damp-
111 ing matrix is applied by means of Rayleigh damping, and the combined damping ratio
112 of soil damping and structural damping is assumed to be 1% (Chen and Duffour, 2018).
113 The Rayleigh mass and stiffness coefficients α_1 and α_2 are defined by $\alpha_1 = \alpha_2 =$

114 $\frac{\zeta_c}{\frac{1}{2\omega} + \frac{\omega}{2}}$. ω is the natural frequency of the first fore-aft mode, and ζ_c is the combined
 115 damping ratio. The RNA is represented by a lumped mass at the tower top.



116

117 Fig. 1. Schematic of NREL 5MW wind turbine and scour effect

118 The TMD is mounted on the top of the tower, and the effect of the TMD is consid-
 119 ered by adding its mass, damping, and stiffness terms at relevant positions in the local
 120 mass, damping, and stiffness matrices of the beam element representing the tower top.
 121 The equation of motion of the OWT main structure is:

$$\begin{aligned} \mathbf{M}_s \ddot{\mathbf{U}}_s + \mathbf{C}_s \dot{\mathbf{U}}_s + \mathbf{K}_s \mathbf{U}_s + \mathbf{C}_T (\dot{\mathbf{U}}_s - \dot{\mathbf{U}}_T) + \mathbf{K}_T (\mathbf{U}_s - \mathbf{U}_T) \\ = \mathbf{F}_{\text{wind}} + \mathbf{F}_{\text{wave}}, \end{aligned} \quad (1)$$

122 where \mathbf{M}_s , \mathbf{C}_s , \mathbf{K}_s are the mass, damping and stiffness matrices of the main structure.
 123 \mathbf{C}_T , \mathbf{K}_T are matrices with same dimensions containing c_T, k_T . \mathbf{U}_s is the displacement
 124 vector of the main structure, and \mathbf{U}_T is the displacement vector containing u_T . \mathbf{F}_{wind} ,
 125 \mathbf{F}_{wave} are the aerodynamic and wave load vectors. The equation of motion for the TMD
 126 can be represented by

$$m_T \ddot{u}_T + c_T (\dot{u}_T - \dot{u}_{s-top}) + k_T (u_T - u_{s-top}) = 0, \quad (2)$$

127 where m_T , c_T , k_T are the mass, damping and stiffness of the TMD, u_T , u_{s-top} are the
 128 displacement of the TMD and the displacement of the top node. The modelling of SSI
 129 is realized by an equivalent stiffness matrix, which will be introduced in detail subse-
 130 quently in Section 2.3.

131 Table 1. Basic properties of the NREL 5MW reference OWT (J. Jonkman et al.,
 132 2009; Rezaei, 2017)

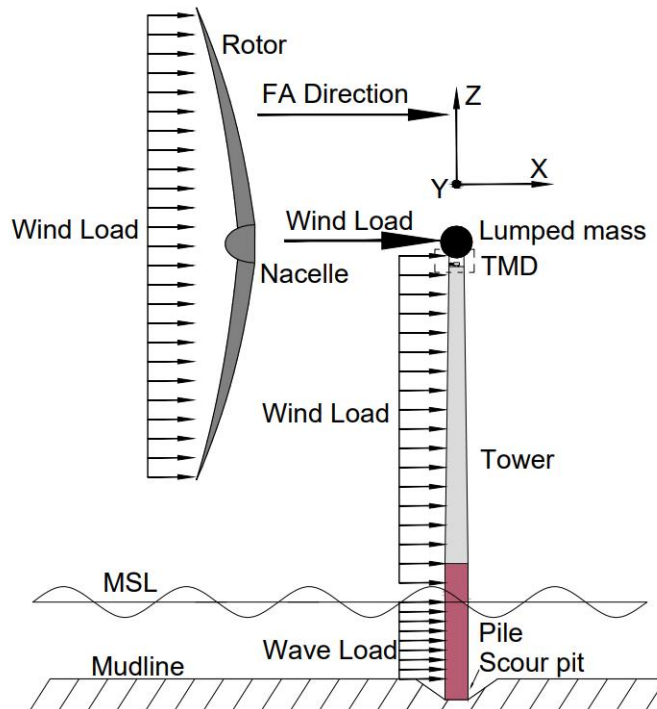
Number of blade	3
Rotor diameter	126 m
Tower length	80 m
Tower diameter	3.87–6.00 m
Tower thickness	28–38 mm
Pile length	75 m
Pile penetration depth	45 m
Pile diameter	6 m
Pile thickness	80 mm
Hub height from MSL	92.4 m
Turbine mass	350000 kg
Blade mass	17740 kg
Rated wind speed	12.1 m/s

133 Wind loads were calculated using modified unsteady blade element momentum
 134 (BEM) theory (Branlard, 2017; B. J. Jonkman and Buhl, 2006) with Prandtl and Glauert
 135 corrections. Ignoring the iterative loop (Chen, Duffour, Fromme, et al., 2021) in the
 136 steady-state BEM code, the instantaneous aerodynamic forces were calculated for each
 137 time step within the time integration. The turbulent wind field was generated using the
 138 Kaimal spectrum according to the wind field parameters of IEC 61400-3 (2019) as-
 139 suming moderate turbulence intensity. It should be noted that the aerodynamic loads
 140 from the rotor applied at the tower top were calculated using an aerodynamic force
 141 linearization technique previously developed by authors (Chen, Duffour, Fromme, et
 142 al., 2021; Chen et al., 2020). This technique divides the aerodynamic loads into two
 143 parts. The first part is the quasi-steady aerodynamic force calculated by BEM theory,
 144 which does not consider the influence of tower top motion. The second part considers
 145 the effect of aerodynamic damping by introducing an additional aerodynamic damping
 146 matrix. The adoption of this technique is to enable the development of the simplified

147 modal model for rapid fatigue calculation, which will be introduced in detail in Sub-
 148 section 2.4. To represent the influence of controller in the OWT, a standard relationship
 149 (J. Jonkman et al., 2009) between the mean wind speed, rotor rotation speed and blade
 150 pitch angles, which represents the OWT's normal operational conditions, are adopted
 151 throughout the wind loading calculation. Wave loads were calculated using the Morison
 152 equation, which includes viscous drag and inertial forces:

$$\mathbf{F}_{\text{wave}} = \frac{1}{2} \rho_w D_{\text{pile}} C_d |\dot{\mathbf{u}}_w| \dot{\mathbf{u}}_w + \frac{\pi}{4} \rho_w D_{\text{pile}}^2 C_m \ddot{\mathbf{u}}_w, \quad (3)$$

153 where $\dot{\mathbf{u}}_w$ and $\ddot{\mathbf{u}}_w$ are the velocity and acceleration of water particles, C_d is the drag
 154 coefficient, D_{pile} is the diameter of the monopile between the mean sea level and the
 155 mudline, C_m is the inertia coefficient and ρ_w is the density of water. C_d and C_m were
 156 chosen as 1 and 2 respectively as the recommended values in Shirzadeh et al (2013).
 157 The wave profiles were obtained through the superposition of wave components, combin-
 158 ing linear wave theory and JONSWAP spectra (Klaus et al., 1973). The application
 159 of wind and wave loads is shown in Fig. 2.



160

161

Fig. 2 Schematic of wind turbine load application

162 **2.2 Scour modelling in ABAQUS**

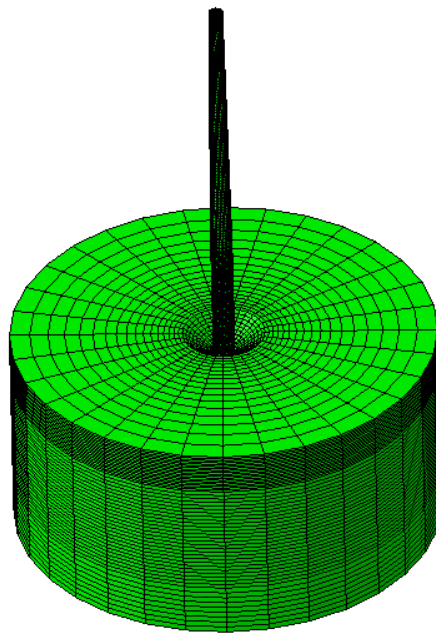
163 Using solid elements to model pile-soil interaction (S. Dai et al., 2021; Fard et al.,
164 2022; Ma and Chen, 2021; Zdravković et al., 2015) is usually considered to be more
165 accurate than the p-y curve method (Liang et al., 2018; Song and Achmus, 2023) and
166 the equivalent embedding method (Shahmohammadi and Shabakhty, 2020; Bergua et
167 al., 2022). The solid element method can also reduce the influence of empirical formula
168 on the results. Therefore, the solid element method is used to establish the wind turbine
169 scour model. The wind turbine scour model established in ABAQUS contains soil, pile
170 foundation, tower, and the RNA is replaced by a concentrated mass located at the top
171 of the tower. The diameter of the soil body is selected as 20 times of the pile diameter,
172 the soil under the pile foundation is selected as 2.5 times of the pile diameter, and the
173 total height of the soil body is 60 m. The soil body is made of homogeneous dense
174 sandy soil, and the piles and tower are made of steel. The material parameters of the
175 soil body, pile and tower are shown in Table 2 below:

176 Table 2. Soil, pile and tower material parameters

Type	Weight γ (kN/m ³)	modulus of elasticity E_s (MPa)	Poisson's ratio ν	Internal friction angle φ (°)	Expansion angle ψ (°)	Cohesion c (kPa)
Soil	19	80	0.3	35	23	0.1
Pile	78.5	215	0.25	-	-	-
Tower	85	215	0.25	-	-	-

177 The Mohr-Coulomb model is used for the soil, and the pile, tower, and nacelle are
178 assumed to be elastic as they are much stiffer than the soil and do not deform plastically
179 for the normal operational conditions. The pile and tower are connected by a binding
180 relationship. The normal contact between the pile and soil adopts the hard contact, and
181 the tangential contact adopts the friction penalty function. The relative sliding friction
182 factor at the interface, μ is equal to $\tan(0.75 \varphi)$, where φ is the internal friction angle.
183 The pile-soil contact is in the form of frictional contact, where mutual contact pairs are
184 established between the pile and the soil, including the contacts between the pile bottom
185 surface and the soil, between the outside surface of the pile and the soil, and the inside
186 surface of the pile and the soil core. The frictional contact between pile bottom surface
187 and soil is omitted due to the small area of the contact surface. These frictional contacts
188 all adopt the face-to-face contact, and the contact discretization method adopts the face-

189 to-face discretization method, considering the large stiffness of the main surface and
190 small stiffness of the slave surface. The perimeter of the soil body is translationally
191 constrained, and the bottom surface of the soil adopts a fixed constraint. The eight-node
192 linear brick element (C3D8R) is used to model the pile and soil, and the mesh division
193 is realized by arranging seeds as shown in Fig. 2. The whole model is set up by adopting
194 the modelling method of “element birth and death”, which realizes the operation of
195 initial soil stress balance and sets up contacts and other related steps by killing and
196 activating relevant elements.



197

198 Fig. 3. Pile-soil interaction modelled by ABAQUS

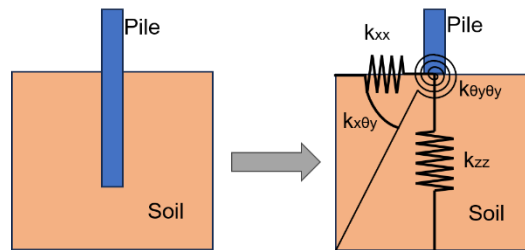
199 The scour conditions can be represented by a deep conical pit around the pile under
200 the long-term action of the waves and currents. According to the specification of Det
201 Norske Veritas (DNV) (2014b), the radius of the pit surface formed by scour, R, can
202 be related to the depth of the scour pit by

$$R = \frac{D}{2} + \frac{S}{\tan\varphi}, \quad (4)$$

203 where D is the diameter of the pile, S is the scour depth, and φ is the angle of internal
204 friction of the soil.

205 **2.3 Equivalent stiffness matrix method**

206 It is necessary to consider the effect of scour in the FE model in MATLAB. An
207 equivalent stiffness matrix method is adopted in the FE model to consider the flexibility
208 induced by SSI. The 6 DOFs of node at the mudline are assumed to be constrained by
209 a series of coupled springs, and the stiffnesses of the coupled springs form a 6×6 stiff-
210 ness matrix. For one specific stiffness term used in the FE model, for instance the one
211 relevant to the lateral displacement in the fore-aft (FA) direction, the value of the stiff-
212 ness term can be found from the relationship between the reaction force at the mudline
213 and the pile top displacement (Jung et al., 2015). The equivalent stiffness schematic of
214 the pile-soil interaction in the FA direction for the OWT is shown in Fig. 4.



215

216 Fig. 4. Equivalent stiffness schematic of pile-soil interaction in the FA direction

217 According to the principle of virtual displacement and with the DOFs in the other
218 directions constrained, a unit displacement or rotation was first applied in one direction,
219 and then the reaction force in that direction can be known. The equivalent stiffness in
220 that direction can be subsequently calculated by the relationship between the displace-
221 ment and reaction force. Using the same approach, the stiffness terms corresponding to
222 the remaining five DOFs were calculated. The stiffness terms in all the six DOFs to-
223 gether form all the diagonal terms of the soil stiffness matrix. With the diagonal terms
224 known, the off-diagonal stiffness terms can be found by applying a unit displacement
225 in one direction and looking at the reaction force in the other concerned direction, with
226 the other four DOFs constrained. Using the same principle, the off-diagonal terms can
227 also be found from the relationship between the displacements and reaction forces,
228 which ultimately results in a 6×6 stiffness matrix (Bergua et al., 2021; Pedersen and
229 Askheim, 2021):

$$\mathbf{F}_{\text{soil}} = \begin{Bmatrix} F_x(t) \\ F_y(t) \\ F_z(t) \\ M_x(t) \\ M_y(t) \\ M_z(t) \end{Bmatrix} = \begin{bmatrix} k_{xx} & 0 & 0 & 0 & k_{x\theta y} & 0 \\ 0 & k_{yy} & 0 & k_{y\theta x} & 0 & 0 \\ 0 & 0 & k_{zz} & 0 & 0 & 0 \\ 0 & k_{\theta xy} & 0 & k_{\theta x\theta x} & 0 & 0 \\ k_{\theta yx} & 0 & 0 & 0 & k_{\theta y\theta y} & 0 \\ 0 & 0 & 0 & 0 & 0 & k_{\theta z\theta z} \end{bmatrix} \begin{Bmatrix} u_x(t) \\ u_y(t) \\ u_z(t) \\ \theta_x(t) \\ \theta_y(t) \\ \theta_z(t) \end{Bmatrix} \quad (5)$$

$$= \mathbf{K}_{\text{soil}} \mathbf{u}_{\text{soil}},$$

230 where \mathbf{K}_{soil} is the equivalent soil stiffness matrix, \mathbf{u}_{soil} is the displacement vector, and
 231 \mathbf{F}_{soil} is the reaction force vector. The 6×6 soil stiffness matrix obtained from ABAQUS
 232 is imported to the FE model in MATLAB. This modelling method possesses the ad-
 233 vantages of the increase in accuracy brought by the scour model in ABAQUS with solid
 234 elements, and the fast calculation speed and convenience in applying wind and wave
 235 loads brought by the usage of the FE model in MATLAB.

236 2.4 Rapid fatigue evaluation method

237 The established FE model in MATLAB can generate dynamic responses of the
 238 OWT, considering wind and wave loads and scour effect. However, a comprehensive
 239 fatigue life prediction in time domain needs to consider a large number of environmen-
 240 tal states and load cases, so simulation efficiency is very important. Moreover, the TMD
 241 design optimization requires much more dynamic response time series. The FE model
 242 is not fast enough in this case. Therefore, a simplified modal model is developed from
 243 the FE model in MATLAB following the method develop in Ref. (C .Chen et al., 2021).
 244 The total aerodynamic forces from the rotor applied on the tower top node are linearized
 245 to the sum of a term corresponding to the forces for an assumed rigid tower, plus a term
 246 proportional to the tower top linear and angular velocities. The hydrodynamic forces
 247 are linearized by ignoring the relatively small monopile vibrations. The details for force
 248 linearization can be found in the authors' previous studies (Chen, Duffour, Fromme, et
 249 al., 2021). Since the dynamic responses of the OWT are mainly dominated by the first
 250 two bending vibration modes, the FE model is reduced into a 4-DOF simplified modal
 251 model by considering only the first two bending modes in the FA and side-side (SS)
 252 directions respectively. The development of the simplified 4-DOF modal model is
 253 briefly introduced as follows. Denoting the mass matrix and stiffness matrix of the
 254 OWT as \mathbf{M} and \mathbf{K} including the TMD and the lumped soil stiffness matrix, the un-
 255 damped vibration mode matrix Ψ can be obtained directly through eigen analysis.

256 According to relationship $\mathbf{u} = \Psi\alpha$ and multiplying the transpose of the undamped vi-
 257 bration matrix Ψ^T with the equation of motion, the following equation is obtained:

$$\Psi^T \mathbf{M} \Psi \ddot{\alpha} + \Psi^T \mathbf{C} \Psi \dot{\alpha} + \Psi^T \mathbf{K} \Psi \alpha = \Psi^T \mathbf{F}. \quad (6)$$

258 Then rewrite the above equation as

$$\bar{\mathbf{M}} \ddot{\alpha} + \bar{\mathbf{C}} \dot{\alpha} + \bar{\mathbf{K}} \alpha = \bar{\mathbf{F}}, \quad (7)$$

259 where α is the general coordinate vector, $\bar{\mathbf{M}}$ is the modal mass matrix, $\bar{\mathbf{C}}$ is the modal
 260 damping matrix, $\bar{\mathbf{K}}$ is the modal stiffness matrix, $\bar{\mathbf{F}}$ the modal load matrix. Truncating
 261 Eq. (6) by only considering the first two bending modes, the FE model is reduced to a
 262 4-DOF modal model, which can be used for a rapid fatigue analysis. The dynamic re-
 263 sponses of the OWT can be obtained by modal superposition after solving the general
 264 coordinate vector by time integration. In the 4-DOF simplified modal model, the cross-
 265 section stress at any height can be calculated from the calculated node displacements.
 266 According to the dynamic stress extraction method provided by Pelayo et al. (Pelayo et
 267 al., 2015), the cross-section stress $\sigma_z(t)$ at any moment at a given location can be ob-
 268 tained by:

$$\sigma_z(t) = -E(\mathbf{N}^{e''}(z)\mathbf{u}_x^e(t)x + \mathbf{N}^{e''}(z)\mathbf{u}_y^e(t)y), \quad (8)$$

269 where \mathbf{u}^e is the nodal displacement vector at the cross section, E is the material elastic
 270 modulus, and \mathbf{N}^e is the elemental shape function vector of FE model, x and y are the
 271 positions within the section at the height z of the tower. After cyclic counting the stress
 272 time series using the rainfall counting method, the fatigue damage at the hotspot can be
 273 evaluated by utilizing the Palmgren-Miner rule based on the S-N fatigue calculation
 274 method. The S-N curve for steel under water can be obtained by the following equation
 275 considering the thickness effect in DNV (2014a):

$$\log N = \log \bar{a} - m \cdot \log \left[\Delta \sigma \left(\frac{t}{t_{\text{ref}}} \right)^k \right], \quad (9)$$

276 where N is the number of cycles to failure, $\Delta \sigma$ is the stress range. $\Delta \sigma$ is calculated from
 277 the nominal stress $\Delta \sigma_{\text{nominal}}$ by the equation $\Delta \sigma = \text{SCF} \cdot \Delta \sigma_{\text{nominal}}$, SCF is the stress
 278 concentration factor. m is the negative inverse slope of the S-N curve, and $\log \bar{a}$ is the

279 intercept between the log N axis and the S-N curve, t_{ref} is the reference thickness for
 280 welded joints, t is the thickness at which cracks may grow and k is the thickness expo-
 281 nent of fatigue strength. For pile joints, $t_{ref} = 25\text{mm}$. According to the DNV code, a
 282 bilinear S-N curve is usually used for offshore structures subjected mainly to typical
 283 wind and wave loads, using the Class E structural detail S-N curve shown in Table 3.

284 Table 3 Class E structural detail S-N curves

$N \leq 10^6$		$N \geq 10^6$			t (mm)	SCF
m_1	$\log \bar{a}_1$	m_2	$\log \bar{a}_2$	k		
3.0	11.610	5.0	15.350	0.2	80	1.13

285 For variable amplitude stresses, the fatigue damage index is calculated using the
 286 Palmgren-Miner summation rule:

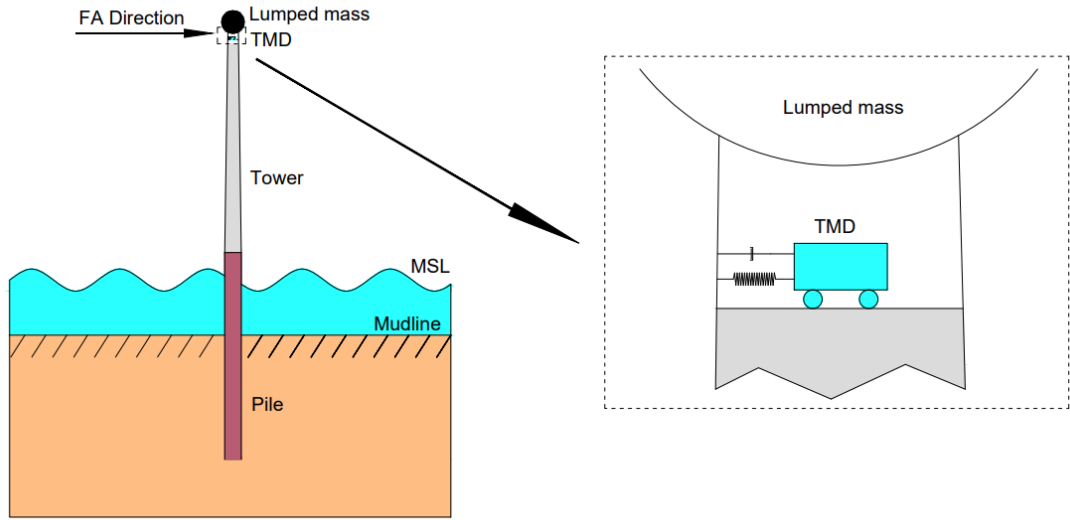
$$D_k = \sum_{i=1}^{N_c} \frac{n_i}{N_i}, \quad (10)$$

287 where N_c is the total number of bins obtained by rainflow counting, n_i is the number of
 288 cycles in stress range i , N_i is the number of cycles to failure in stress range i , and D_k is
 289 the total fatigue damage index. Fatigue failure occurs at the hotspot when the fatigue
 290 damage index reaches unit 1.

291 3 Damper design and optimisation method

292 Installing damping devices can efficiently reduce the vibration amplitudes of
 293 OWTs so that their service life can be greatly prolonged. Using TMDs as passive con-
 294 trol devices is most widely used to control the vibration of OWT support structures.
 295 Usually, most of TMDs are designed according to the dynamic characteristics of the
 296 OWTs determined in the preliminary design stage, without considering the changes in
 297 dynamic properties possibly caused by scour and soil degradation. However, in the real
 298 environment, scour can cause the dynamic characteristics of OWTs to change, which
 299 perhaps makes installed dampers become less effective or even completely ineffective.
 300 Therefore, it is a great significance to consider the change in dynamic properties caused
 301 by scour on the TMD design. The following two subsections first introduce the tradi-
 302 tional TMD design method considering constant dynamic characteristic in the initial
 303 state, and then an optimal parameter searching method for the design of TMDs is pre-
 304 sented considering the effect of scour and fatigue life evaluation.

305 3.1 TMD design in initial state



306

307 Fig. 5. Schematic diagram of TMD arrangement in the tower tube

308 As the dominant vibration mode of the OWT structure in operation is the first
 309 bending mode, the largest vibration amplitude occurs at the tower top and installing the
 310 TMD at the tower top is most effective. Therefore, the TMD is installed inside the steel
 311 tube at the tower top to mainly control the vibration in the FA direction, as shown in
 312 Fig. 5. Accordingly, the initial design of the TMD is mainly carried out based on the
 313 dynamic properties for the first-order mode. The initial design is conduct based on the
 314 assumption that the monopile foundation is not scoured.

315 Numerous studies have shown that a TMD can effectively suppress the vibration
 316 of a main structure when the mass ratio of the TMDs to the main structure is 1%-2%
 317 (Lackner and Rotea, 2011b; R. Zhang et al., 2019). After determining the mass ratio of
 318 the TMD to the OWT structure, according to the classic TMD optimization theory
 319 proposed by Den Hartog (1957), the optimal frequency ratio of the TMD to the OWT
 320 structure is

$$\alpha_{\text{opt}} = \frac{1}{1 + \mu}. \quad (11)$$

321 The optimal damping ratio for the TMD can be calculated by

$$\xi_{\text{opt}} = \sqrt{\frac{3\mu}{8(1 + \mu)}}, \quad (12)$$

322 where μ is the mass ratio of the TMD to the OWT structure, α_{opt} is the optimal fre-
 323 quency ratio of the TMD to the OWT structure and α_{opt} is the optimal damping ratio
 324 of the TMD.

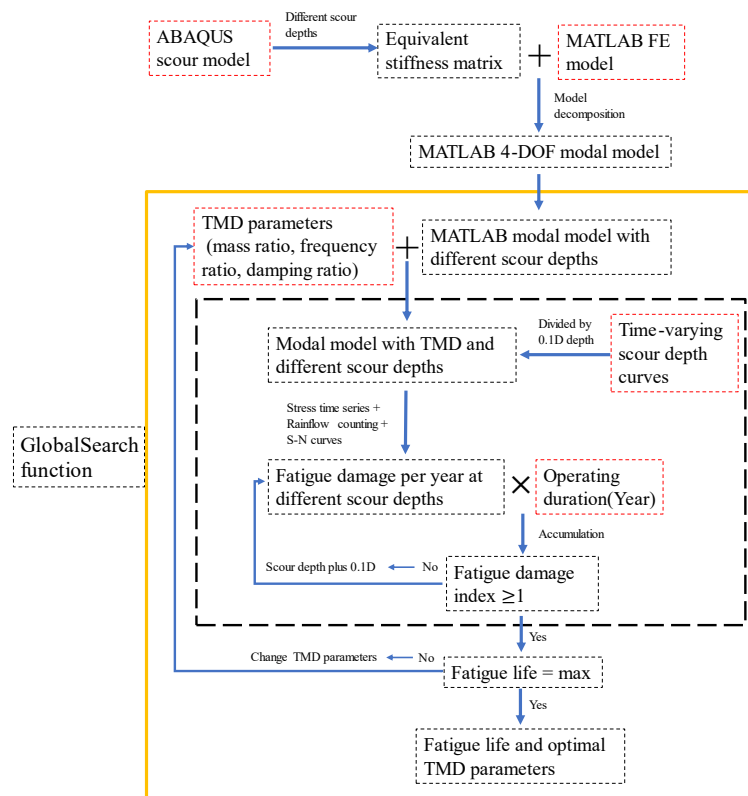
325 Considering that excessive mass will lead to increased construction costs and dif-
 326 ficulties and changes in the inherent characteristics of the original structure, the mass
 327 ratio of the TMD system to the main structure is first selected to be 1%. Moreover,
 328 previous studies have found that TLCD with a mass ratio of 1% and TMD with a mass
 329 ratio of 2% can effectively suppress vibration (Colwell and Basu, 2009; Lackner and
 330 Rotea, 2011b; R. Zhang et al., 2019). According to Den Hartog's optimization theory
 331 for the initial TMD design, it can be determined that the optimal frequency ratio of the
 332 TMD to the main structure is 0.99, and the optimal damping ratio of the TMD is 0.061.
 333 When the OWT support structure is not scoured, the first-order modal mass of the struc-
 334 ture is 440350 kg, and the first-order modal frequency is 0.265 Hz. Therefore, accord-
 335 ing to the initial design parameters, the mass, stiffness coefficient and damping coeffi-
 336 cient of the TMD system are 4403.5 kg, 11,952 N/m and 885 Ns/m respectively.

337 3.2 Fatigue-based damper optimisation technique

338 After scour occurs around the monopile foundation, the burial depth of the mono-
 339 pile and natural frequencies of the OWT gradually change. The vibration mitigation
 340 effect of the TMD designed based on the dynamic parameters in the initial state can be
 341 reduced, which may lead to the increase of fatigue damage of the OWT support struc-
 342 ture. Therefore, when designing the TMD, considering the influence of the time-vary-
 343 ing scour can enhance the performance of the TMD and thus result in a longer fatigue
 344 life of the support structure.

345 Here a fatigue-life-based optimization technique (FOT) to find optimal parameters
 346 of the TMD is developed in MATLAB as shown in Fig. 8. In this technique, the fre-
 347 quency ratio, mass ratio and damping ratio of the TMD are set as the optimal parameters
 348 to search, and the fatigue life is the optimization objective. When considering the time-
 349 varying scour process, the time-varying scour depth curve is first divided into a number
 350 of scour depths with an increment of 0.1d. For each scour depth, the fatigue damage is

351 calculated respectively and then the total fatigue damage in a particular duration can be
 352 summarised. When the scour pit becomes deeper, the fatigue damage accumulates and
 353 finally reaches unit 1 which denotes the end of fatigue life. The simplified 4-DOF modal
 354 model incorporating scour modelling is used to generate the stress time series. The op-
 355 timization problem is formed so that the optimal parameters of the TMD correspond to
 356 the longest fatigue life of the OWT support structure. The GlobalSearch function in
 357 MATLAB was used to solve the optimization problem. In the TMD optimization pro-
 358 cess, the mass ratio of TMD is first set to 1%, and only the parameter frequency ratio
 359 and damping ratio are optimized. Subsequently, in order to understand the optimization
 360 effect of TMD when the value of TMD mass ratio is not fixed, a mass ratio optimization
 361 interval is given, so the mass ratio becomes a variable within the optimization interval.



362
 363 Fig. 6. Flowchart of TMD fatigue-life-based optimization technique

364 4 Results

365 4.1 Environmental states and load cases

366 In this study, fatigue analyses are performed under 22 environmental states pro-
 367 vided by Tempel (2006), taking into account both operational and parked conditions.
 368 These 22 environmental states are shown in Table 4. The wind and wave loads are
 369 assumed to be always in the same direction to simplify the analysis. When the mean

370 wind speeds are above the cut-in wind speed and below the cut-out wind speed, a 95%
 371 wind turbine availability is assumed following the setting in Ref (Velarde et al., 2020),
 372 meaning that the OWT does not produce power for 5% when the mean wind speeds are
 373 in the operating range. For a particular set of mean wind speed, wave period and wave
 374 height, six different random seed numbers are used to generate different wind fields
 375 and wave profiles to reduce the influence of randomness. To obtain the stress time his-
 376 tories at the mudline, a 700s simulation for each random seed was conducted and the
 377 response in the first 100 seconds was deducted to eliminate the effect of initial transient
 378 vibration. (Capaldo and Mella, 2023; Stieng and Muskulus, 2020).

379 Table 4. Environmental states, adopted from Tempel (van der Tempel, 2006).

State	V _w (m/s)	T _z (s)	H _s (m)	P _{State} (%)	State	V _w (m/s)	T _z (s)	H _s (m)	P _{State} (%)
1	4	3	0.5	3.95	12	14	5	2	3.26
2	4	4	0.5	3.21	13	16	4	2	1.79
3	6	3	0.5	11.17	14	16	5	2.5	3.1
4	6	4	0.5	7.22	15	18	5	2.5	1.74
5	8	3	0.5	11.45	16	18	5	3	0.8
6	8	4	1	8.68	17	20	5	2.5	0.43
7	10	3	0.5	5.31	18	20	5	3	1.14
8	10	4	1	11.33	19	22	5	3	0.4
9	12	4	1	5.86	20	22	6	4	0.29
10	12	4	1.5	6	21	24	5	3.5	0.15
11	14	4	1.5	4.48	22	24	6	4	0.1

380 In Table 4, V_w is the wind speed, T_z is the zero-crossing wave period, H_s is the
 381 wave height, and P_{state} is the probability of environmental state. To investigate the ef-
 382 fect of scour and installation of the TMD on the fatigue damage accumulation, six load
 383 cases (LCs) are selected as shown in Table 5. LC 1 is used as the reference case, and
 384 other cases are distinguished by different scour and TMD settings. For LC 4 to LC 6,
 385 the initial design of the TMD with the mass ratio of 1% is used.

386 Table 5. Load case definition

LC number	TMD condition	Scour condition	LC number	TMD condition	Scour condition
LC 1	No	No Scour	LC 4	Enable	No Scour
LC 2	No	Time-varying	LC 5	Enable	Time-varying
LC 3	No	Maximum	LC 6	Enable	Maximum

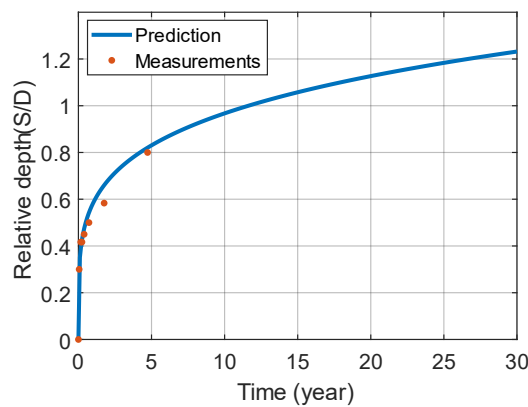
387 When considering the time-varying scour depth, for a particular time t , the time-
 388 varying scour depth S can be predicted by the equation provided by Nakagawa et al.
 389 (1976):

$$S = \left(\frac{t}{t_1}\right)^{0.22} D, \quad (13)$$

390 where D is the diameter of the monopile, t_1 is the reference time and can be calculated
 391 by

$$t_1 = 29.2 \cdot \frac{D}{\sqrt{2} \cdot u} \cdot \left(\frac{\sqrt{\Delta \cdot g \cdot d_{50}}}{\sqrt{2} \cdot u - u_c}\right)^3 \cdot \left(\frac{D}{d_{50}}\right)^{1.9}. \quad (14)$$

392 u is the tidal velocity and taken as 0.5 m/s, u_c is the critical shear velocity and taken as
 393 0.37 m/s, g is the acceleration of gravity and taken as 9.8 m/s², d_{50} is grain size of sea
 394 sand and taken as 0.2 mm. The parameter $\Delta = \frac{\rho_s}{\rho_w} - 1$, where ρ_s is density of sand and
 395 taken as 2.65 g/cm³, ρ_w is density of water and taken as 1 g/cm³. Rudolph et al. (Ru-
 396 dolph et al., 2016) provided the sea state and measured the scour depth for the North
 397 Sea where the monopile N7 is located. The measured scour depth was fitted well for
 398 the first five years based on the time-varying scour depth prediction equation shown in
 399 Eq. (13). Therefore, the data from the North Sea site can represent a typical ocean en-
 400 vironment with time-varying scour and is used for the correlation analysis in this study.



401

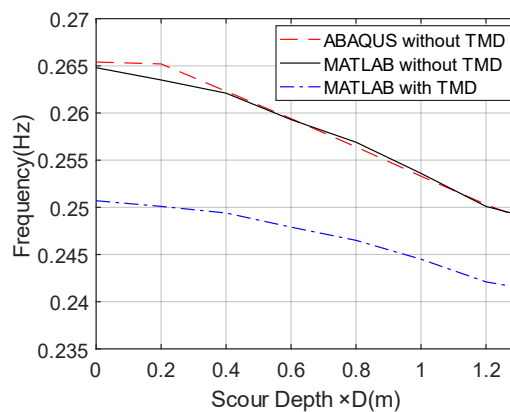
402 Fig. 7. Time-varying scour depth curve for pile N7 in the North Sea

403 When conducting analysis with the time-varying scour, an increment of scour
 404 depth equal to 0.1D is used. At one particular scour depth, the fatigue damage is calcu-
 405 lated and then the total fatigue damage during a longer period with a changing scour

406 depth can be obtained by damage accumulation. According to the specification of DNV,
407 the maximum depth of a local scour pit formed around a pile foundation is 1.3 times
408 the diameter of the pile. Therefore, it is assumed that the local scour pit has a maximum
409 scour depth of $1.3D$ at which the scour process achieves equilibrium.

410 4.2 Scour influence on natural frequencies

411 The scour of the soil around the monopile has an important effect on the natural
412 frequencies of the OWT. For different scour depths, the first natural frequencies ob-
413 tained the by the models in ABAQUS and MATLAB are compared in Fig. 8. It shows
414 the increase in the scour depth leads to a decrease in the first natural frequency of the
415 OWT. The first natural frequency is 0.265 Hz when no scour occurs, and the natural
416 frequency is reduced to 0.248 Hz when the depth of the scour pit reaches the maximum
417 depth. The first natural frequency is reduced by 6.42% due to the maximum scour depth.
418 It shows that the natural frequency nearly monotonically decreases with the increase of
419 the scour depth. The installation of TMD also influences the natural frequency of the
420 OWT main structure. The TMD with a mass ratio of 1% makes the first natural fre-
421 quency of the OWT main structure reduces to 0.251 Hz when no scour occurs, meaning
422 that the natural frequency is reduced by 5.28%.

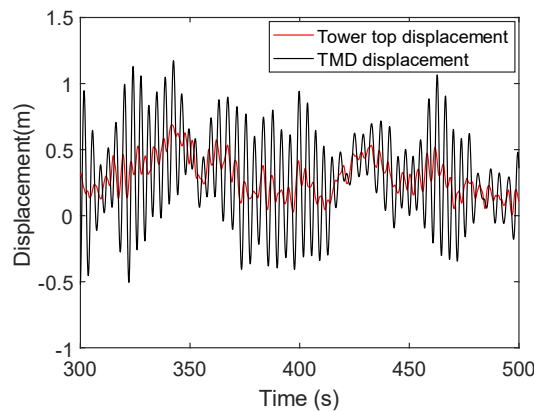


423

424 Fig. 8. Relationship between wind turbine natural frequency and scour depth

425 In the TMD design process, the feasible displacement should be considered. The
426 smaller the mass ratio of TMD is, the larger the feasible displacement is required. The
427 22nd environmental state corresponds to the greatest vibration responses of the wind
428 turbine tower top due to large wind speed variations and lower aerodynamic damping,
429 and the stroke of the TMD could be the largest. As shown in the Fig. 9, the relative
430 displacement between the TMD and the tower top is much less than the inner diameter

431 of the wind turbine tower top in the 22nd environmental state. It shows that the stroke
432 of the TMD is sufficient when the mass ratio of TMD is 1%.

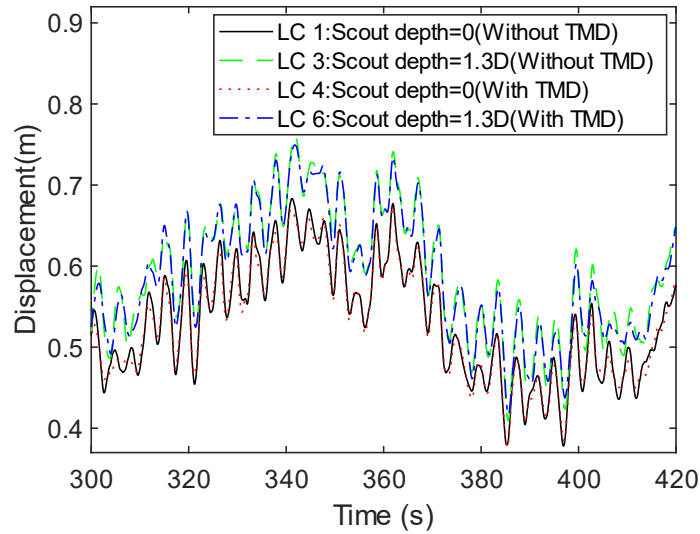


433

434 Fig. 9 Displacement of tower top and TMD under the 22nd environmental state

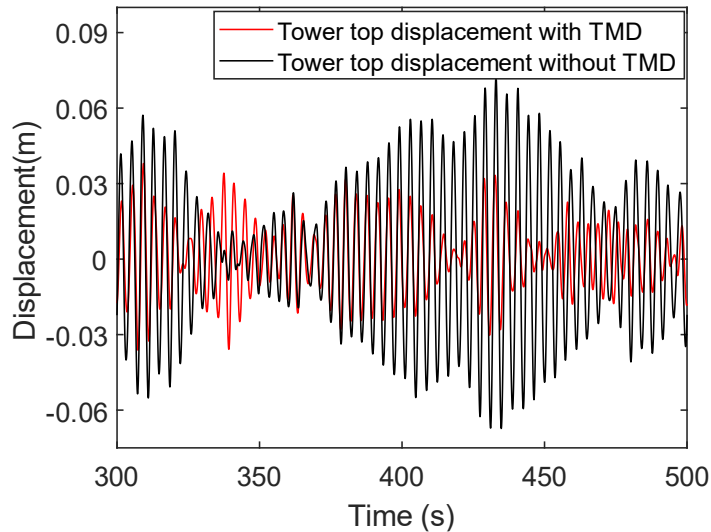
435 4.3 Dynamic response analysis

436 When the OWT in the operating state is under the 9th environmental state which
437 corresponds to the rated wind speed of 12 m/s, a comparison for the tower top displacements
438 is made for LC 1, LC 3, LC 4 and LC 6, as shown in Fig. 10. These displacements
439 are obtained from the FE model in MATLAB described in Subsection 2.1. By comparing
440 the displacements from 300 seconds to 420 seconds for LC 1 and LC 4, it can be
441 found that the displacement amplitudes of the tower top decreases when the TMD is
442 installed. It is known that the aerodynamic damping is large when the OWT is operating
443 under the rated wind speed, so it is normal that the vibration mitigation effect of the
444 TMD is less significant in this case. The effect of the TMD is more prominent for
445 parked conditions with less aerodynamic damping. As shown in the Fig. 11, the vibration
446 mitigation effect of the TMD is more significant under the parked condition with
447 3 m/s wind speed. Moreover, by comparing the displacement responses for LC 1 and
448 LC 3, it can be found that the average of the displacement at the tower top increases
449 when the scour depth reaches 1.3D. This is because scour makes the OWT support
450 structure become more flexible.



451

452 Fig. 10. Dynamic response of wind turbine under wind-wave coupled loads for four
 453 operating conditions



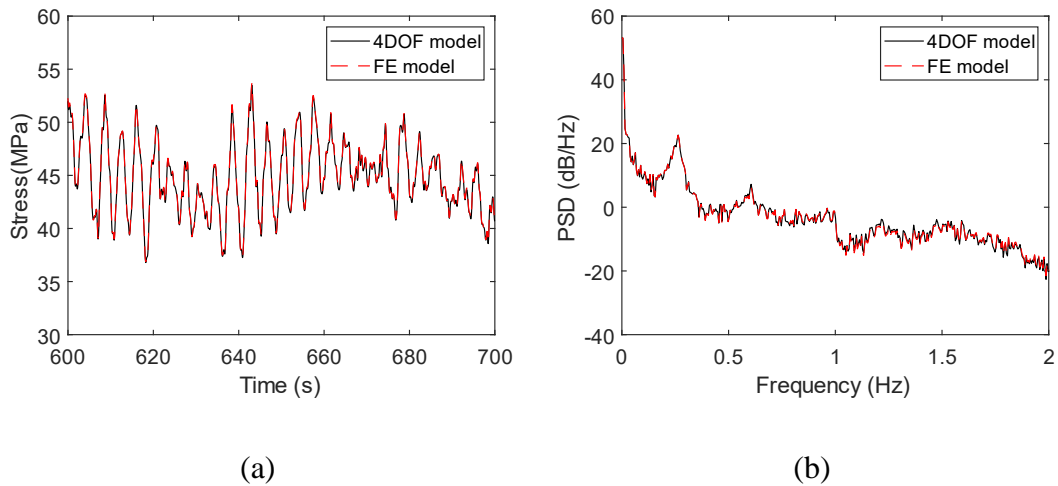
454

455 Fig. 11 The displacement response of wind turbine tower under the parked condition
 456 with 3 m/s wind speed

457 **4.4 Fatigue calculation results**

458 In Subsection 2.4, it is mentioned that in the process of fatigue life analysis, the 4-
 459 DOF simplified modal model is used to greatly save the calculation time. The accuracy
 460 test of the 4-DOF modal model in generating dynamic responses is first present in this
 461 subsection. Under the turbulent wind field with a turbulence intensity of 11.9% and an
 462 average wind speed of 12 m/s, the FE model and the 4-DOF simplified modal model
 463 are used to calculate the stress responses at the mudline for 10 minutes.

464 As shown in Fig. 12, the stress responses from these two models are very close,
 465 confirming good accuracy of the 4-DOF modal model. The fatigue damage caused by
 466 the FE model in 10 min is 2.108×10^{-7} , and the fatigue damage caused by the 4-DOF
 467 model in 10 min is 2.1×10^{-7} , with an error of 0.05%. Moreover, the calculation time
 468 of the 4-DOF simplified modal model is only about 1/55 of that of the FE model, which
 469 shows that the 4-DOF simplified modal model is adequate to replace the FE model
 470 when conducting fatigue life prediction.

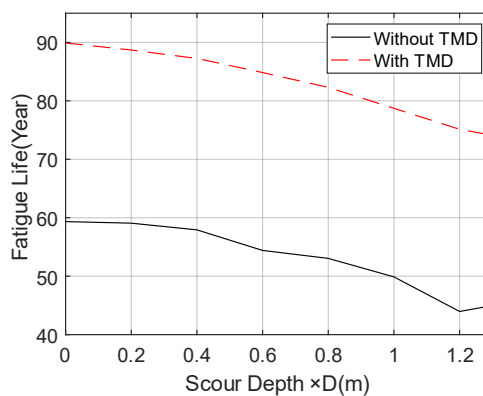


471 Fig. 12. Comparison of stresses at the mudline from the FE model and the 4-DOF
 472 model in time domain (a) and frequency domain (b)

473 The 4-DOF simplified modal model is used to conduct fatigue life prediction for
 474 the OWT support structure under LC 1 to LC 6. A 10 min simulation for each random
 475 seed of is six different random seed numbers conducted to obtain the stress time histo-
 476 ries at the mudline. The location of the hotspot used to evaluate fatigue damage is se-
 477 lected at the point where the maximum stress is reached, and this point is in the support
 478 structure cross section at the mudline. Although the location in the monopile where the
 479 moment reaches its maximum value can be below the mudline, the location at the mud-
 480 line is picked for simplicity. Further, as the SSI is modelled in the FE model by an
 481 equivalent soil stiffness matrix, it is unstraightforward to obtain the internal forces at
 482 the cross sections below the mudline. Given the stress time series at the selected hotspot,
 483 the corresponding fatigue damage is calculated. Then the fatigue damage for the set of
 484 mean wind speed, wave period and wave height in 10 min is obtained by averaging the
 485 fatigue damage for all the six random seeds. For all the 22 environment states, the 10
 486 min fatigue damage are calculated, and the fatigue life is predicted according to

487 Palmgren-Miner sum rule by combing these calculated fatigue damage and the occur-
488 rence probabilities of the environmental states.

489 For different scour depths, the fatigue life of the OWT considering both operating
490 and parked conditions is predicted with or without TMD installation, and the results are
491 shown in Fig. 13. It is shown that an increase in scour depth leads to a decrease in
492 fatigue life, and an increasing fatigue life reduction rate can be observed when the scour
493 depth increases. When no scour occurs and the TMD is not installed on the OWT, the
494 OWT's fatigue life is 59.3 years, and the fatigue life drops to 45.0 years when consid-
495 ering the maximum scour depth of 1.3 D. There exist some uncertainties in the fatigue
496 life prediction process due to the generation of random wind field and wave profile. It
497 should be noted that the predicted fatigue life is much longer than the normally adopted
498 OWTs' design fatigue life of 25-30 years. This can be explained by the following rea-
499 sons. First, the maximum moment of the OWT support structure is not at the cross
500 section at the mudline where the selected hotspot is located. Second, the complex wind
501 and wave directionality during the OWT's lifetime is simplified, which would influence
502 the fatigue calculation result. Third, many other operation conditions such as starting
503 up, shutting down phases are not considered in this study, which can also have an im-
504 pact on the fatigue damage accumulation. Moreover, the installation of the TMD greatly
505 extends about 51.8% of the OWT support structure's fatigue life.



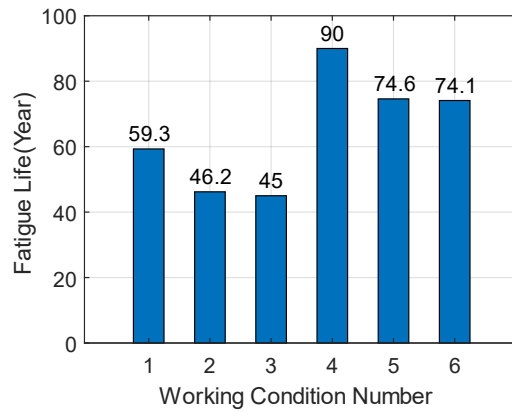
506

507 Fig. 13. Fatigue life of wind turbine with different scour depths

508 The fatigue life prediction results of the OWT were obtained for all the six LCs,
509 as shown in Fig. 14. The fatigue life from the reference case LC 1, 59.3 years, is re-
510 garded as the reference fatigue life. It shows that the fatigue life decreases by 14.3 years,
511 or about 24.1%, when the scour depth is set as the maximum value of 1.3D without
512 applying the TMD, compared to the reference fatigue life. When considering the time-

513 varying scour, the fatigue life decreases by about 22.1% from the reference value. When
 514 comparing the results for LC 1 and LC 4, it shows the installation of the TMD results
 515 in a significant increase in the fatigue life of the OWT, with an increase in fatigue life
 516 of about 30.7 years, which is about 51.8%. In LCs with the TMD installed, the fatigue
 517 life in LC 6 decreases by about 17.7% when the scour depth reaches 1.3 D, compared
 518 to the result in LC 4. But the fatigue life in LC 6 is still 1.25 times of the reference
 519 fatigue life, which indicates that the imposition of TMD can effectively increase the
 520 fatigue life of the OWT by reducing vibration amplitudes.

521



522

Fig. 14. Fatigue life of the wind turbine under six operating conditions

523

4.5 Fatigue calculation with optimized TMD

524

525

526

527

528

529

530

531

532

533

534

To compare the optimization effect and speed up the optimal parameter search process, the mass ratio of TMD is first kept as 1%. Before the optimization, the parameter ranges of the frequency ratio and damping ratio need to be defined. The optimal frequency of the TMD is usually close to the resonance frequency of the main structure, so the range of the frequency ratio was chosen to be from 0.8 to 1.1 for optimization. As the optimal damping ratio could vary in a relatively larger range, the range of the damping ratio for optimization is chosen to be from 1% to 30%. The optimization of the TMD is also conducted with the mass ratio not fixed. A range of the mass ratio from 0.001 to 0.1 is used to optimize the TMD so that the influence of the mass ratio can be evaluated.

Table 6. Optimization of TMD parameters

Optimization method	Mass ratio range	Time-varying scour	Optimal mass ratio	Optimal frequency ratio	Optimal damping ratio	Fatigue life (Year)

Initial (LC 5)	0.01	Use	0.01	0.99	0.061	74.6
FOT	0.01	Use	0.01	0.94	0.050	93.2
FOT	0.001-0.1	Use	0.097	0.92	0.150	133.2

535 The optimal parameters obtained by FOT as well as the predicted fatigue life are
536 listed in Table 6. The fatigue life for LC 5 and the parameters of the initially designed
537 TMD are also shown in Table 6 for comparison. It shows that when the mass ratio is
538 fixed at 1%, the optimal frequency ratio is 0.94, the optimal damping ratio is 5%, and
539 the final fatigue life is 93.2 years. Compared to the fatigue life with initially optimized
540 TMD using the traditional method without considering scour, the fatigue life is in-
541 creased by 18.6 years or about 25%. It indicates that the parameter search in the opti-
542 mization process is correct and it is better to use the TMD parameter search method to
543 design the TMD after obtaining the time-varying scour curve. When the mass ratio
544 range is taken from 0.1% to 10%, the optimal mass ratio of the TMD is 9.7%, the fre-
545 quency ratio is 0.92, the damping ratio is 15%, and the final fatigue life is 133.2 years.
546 In this case, the fatigue life of the OWT is significantly increased mainly due to the
547 large mass ratio. However, in practice, it might be uneconomic to implement a TMD
548 with such a large mass ratio.

549 5 Conclusions

550 This study establishes a rapid numerical model which can consider the effect of
551 scour and installation of a TMD, and the TMD operates only in the FA direction. The
552 model is simplified by using concentrated mass instead of RNA and ignores the non-
553 linearity of the equivalent stiffness matrix. The established model is used to investigate
554 the influence of scour and the installed passive structural control device on the OWT's
555 natural frequencies and fatigue life through 22 environmental states. An optimization
556 technique is also developed to find optimal parameters of the TMD considering time-
557 varying scour. Moreover, it shows that the vibration amplitude of the OWT can be ef-
558 fectively reduced by the TMD. On the one hand, results show that the TMD reduces
559 the vibration amplitude of the tower top. On the other hand, when the scour depth
560 reaches 1.3D, the wind turbine support structure becomes more flexible, with the dis-
561 placement of the tower top increased without TMD.

562 In addition, the fatigue calculation results show that installation of the TMD sig-
563 nificantly extends the fatigue life of the OWT, but scour can cause a reduced perfor-
564 mance of the TMD. It is found that when the initially designed TMD does consider

565 scour and the scour-induced natural frequency reduction during the OWT's lifetime, its
566 performance is not as good as the TMD optimized by the developed FOT in terms of
567 fatigue life enhancement. Given a mass ratio of 1%, the fatigue life can be extended by
568 25% with the TMD optimized by FOT. This is because FOT can consider the effect of
569 time-varying scour. This study only performs the analysis with scour, but other factors
570 such as soil degradation can also alter the dynamic characteristics of OWTs and thus
571 have some influence on structural control devices' performance and fatigue life evalu-
572 ation. Additionally, during OWTs' lifetime, the properties of installed TMDs can also
573 change, making the evaluation of TMDs' performance and OWTs' fatigue life more
574 complicated. These factors are worthwhile investigating in the future.

575 **6 Competing interests**

576 The contact author has declared that none of the authors has any competing inter-
577 ests.

578 **7 Acknowledgements**

579 The financial supports from the National Natural Science Foundation of China (No.
580 52108280), Yangjiang Offshore Wind Laboratory (No. YJOWP-OF-2022A10),
581 the National Science Fund for Distinguished Young Scholars (No. 52025082) are
582 greatly appreciated.

583

584

585

586

587

588

589 **References**

- 590 Amirafshari, P., Brennan, F. and Kolios, A. (2021). A fracture mechanics framework
591 for optimising design and inspection of offshore wind turbine support structures
592 against fatigue failure. *Wind Energy Sci.*, 6(3), 677–699.
593 <https://doi.org/10.5194/wes-6-677-2021>
- 594 Aydin, E., Öztürk, B., Kebeli, Y. E. and Gültepe, G. (2023). An Experimental Study on
595 the Effects of Different Pendulum Damper Designs on Structural Behavior. In
596 G. P. Cimellaro (Ed.), *Seismic Isolation, Energy Dissipation and Active Vibration
597 Control of Structures* (Vol. 309, pp. 240–253). Cham: Springer Interna-
598 tional Publishing. https://doi.org/10.1007/978-3-031-21187-4_18
- 599 Bergua, R., Robertson, A., Jonkman, J. and Platt, A. (2021). Specification Document
600 for OC6 Phase II: Verification of an Advanced Soil-Structure Interaction Model
601 for Offshore Wind Turbines (NREL/TP--5000-79938; p. NREL/TP--5000-
602 79938).
- 603 Bergua, R., Robertson, A., Jonkman, J., Platt, A., Page, A., Qvist, J., Amet, E., Cai, Z.,
604 Han, H., Beardsell, A., et al. (2022). OC6 Phase II: Integration and verification
605 of a new soil–structure interaction model for offshore wind design. *Wind En-
606 ergy*, 25, 793–810.
- 607 Branlard, E. (2017). *Wind Turbine Aerodynamics and Vorticity-Based Methods: Fun-
608 damentals and Recent Applications* (Vol. 7). Cham: Springer International Pub-
609 lishing.
- 610 Capaldo, M. and Mella, P. (2023). Damping analysis of floating offshore wind turbines
611 (FOWTs): a new control strategy reducing the platform vibrations. *Wind En-
612 ergy Sci.*, 8(8), 1319–1339. <https://doi.org/10.5194/wes-8-1319-2023>
- 613 Chen, C. and Duffour, P. (2018). Modelling damping sources in monopile-supported
614 offshore wind turbines. *Wind Energy*, 21(11), 1121–1140.
615 <https://doi.org/10.1002/we.2218>
- 616 Chen, C., Duffour, P., Dai, K., Wang, Y. and Fromme, P. (2021). Identification of aer-
617 odynamic damping matrix for operating wind turbines. *Mech. Syst. Signal Pro-
618 cess.*, 154, 107568. <https://doi.org/10.1016/j.ymssp.2020.107568>
- 619 Chen, C., Duffour, P. and Fromme, P. (2020). Modelling wind turbine tower-rotor in-
620 teraction through an aerodynamic damping matrix. *J. Sound Vib.*, 489, 115667.
621 <https://doi.org/10.1016/j.jsv.2020.115667>
- 622 Chen, C., Duffour, P., Fromme, P. and Hua, X. (2021). Numerically efficient fatigue
623 life prediction of offshore wind turbines using aerodynamic decoupling. *Renew.
624 Energy*, 178, 1421–1434. <https://doi.org/10.1016/j.renene.2021.06.115>
- 625 Colwell, S. and Basu, B. (2009). Tuned liquid column dampers in offshore wind tur-
626 bines for structural control. *Eng. Struct.*, 31(2), 358–368.
627 <https://doi.org/10.1016/j.engstruct.2008.09.001>
- 628 Dai, K., Huang, H., Lu, Y., Meng, J., Mao, Z. and Camara, A. (2021). Effects of soil–
629 structure interaction on the design of tuned mass damper to control the seismic
630 response of wind turbine towers with gravity base. *Wind Energy*, 24(4), 323–
631 344. <https://doi.org/10.1002/we.2576>

- 632 Dai, S., Han, B., Wang, B., Luo, J. and He, B. (2021). Influence of soil scour on lateral
633 behavior of large-diameter offshore wind-turbine monopile and corresponding
634 scour monitoring method. *Ocean Eng.*, 239, 109809.
635 <https://doi.org/10.1016/j.oceaneng.2021.109809>
- 636 Den Hartog, J. P. (1957). *Mechanical Vibrations*. Fourth Edition. *Aeronaut. J.*, 61(554),
637 139–139.
- 638 Dinh, V.-N. and Basu, B. (2015). Passive control of floating offshore wind turbine nacelle
639 and spar vibrations by multiple tuned mass dampers. *Struct. Control Health*
640 *Monit.*, 22(1), 152–176. <https://doi.org/10.1002/stc.1666>
- 641 DNVGL-RP-0005. (2014a). RP-C203: Fatigue design of offshore steel structures.
- 642 DNV-OS-J101. (2014b). Design of Offshore Wind Turbine Structures.
- 643 Fard, M. M., Erken, A., Erkmen, B. and Ansal, A. (2022). Analysis of Offshore Wind
644 Turbine by considering Soil-Pile-Structure Interaction: Effects of Foundation
645 and Sea-Wave Properties. *J. Earthq. Eng.*, 26(14), 7222–7244.
646 <https://doi.org/10.1080/13632469.2021.1961936>
- 647 IEC 61400-3-1. (2019). Wind energy generation systems Part 3-1: Design requirements
648 for fixed offshore wind turbines.
- 649 Jonkman, B. J. and Buhl, M. L. (2006). *TurbSim User's Guide*. Tech. Rep., 500, 39797.
- 650 Jonkman, J., Butterfield, S., Musial, W. and Scott, G. (2009). Definition of a 5-MW
651 Reference Wind Turbine for Offshore System Development (NREL/TP-500-
652 38060, 947422; p. NREL/TP-500-38060, 947422).
- 653 Jung, S., Kim, S.-R., Patil, A. and Hung, L. C. (2015). Effect of monopile foundation
654 modeling on the structural response of a 5-MW offshore wind turbine tower.
655 *Ocean Eng.*, 109, 479–488.
- 656 Klaus, H., Dirk, J. O. and Peter, M. (1973). Measurements of wind-wave growth and
657 swell decay during the joint North Sea wave project (JONSWAP).
- 658 Lackner, M. A. and Rotea, M. A. (2011a). Passive structural control of offshore wind
659 turbines. *Wind Energy*, 14(3), 373–388. <https://doi.org/10.1002/we.426>
- 660 Lackner, M. A. and Rotea, M. A. (2011b). Structural control of floating wind turbines.
661 *Mechatronics*, 21(4), 704–719. <https://doi.org/10.1016/j.mechatronics.2010.11.007>
- 663 Liang, F., Chen, H. and Jia, Y. (2018). Quasi-static p-y hysteresis loop for cyclic lateral
664 response of pile foundations in offshore platforms. *Ocean Eng.*, 148, 62–74.
665 <https://doi.org/10.1016/j.oceaneng.2017.11.024>
- 666 Lu, D., Wang, W. and Li, X. (2023). Experimental study of structural vibration control
667 of 10-MW jacket offshore wind turbines using tuned mass damper under wind
668 and wave loads. *Ocean Eng.*, 288, 116015.
669 <https://doi.org/10.1016/j.oceaneng.2023.116015>
- 670 Ma, H. and Chen, C. (2021). Scour protection assessment of monopile foundation de-
671 sign for offshore wind turbines. *Ocean Eng.*, 231, 109083.
672 <https://doi.org/10.1016/j.oceaneng.2021.109083>

- 673 Mayall, R. O., McAdam, R. A., Byrne, B. W., Burd, H. J., Sheil, B. B., Cassie, P. and
674 Whitehouse, R. J. S. (2018). Experimental modelling of the effects of scour on
675 offshore wind turbine monopile foundations. In A. McNamara, S. Divall, R.
676 Goodey, N. Taylor, S. Stallebrass, and J. Panchal (Eds.), PHYSICAL MODEL-
677 LING IN GEOTECHNICS, VOL 1 (pp. 725–730). Int Soc Soil Mech & Ge-
678 otechn Engn, Tech Comm 104 Phys Modelling Geotechn; Active Dynam;
679 Tekscan.
- 680 Nakagawa, H. and Suzuki, K. (1976). Local Scour Around Bridge Pier in Tidal Current.
681 Coast. Eng. Jpn., 19(1), 89–100.
682 <https://doi.org/10.1080/05785634.1976.11924219>
- 683 Pedersen, D. M. and Askheim, H. (2021). Implementation of seismic soil-structure in-
684 teraction in OpenFAST and application to a 10MW offshore wind turbine on
685 jacket structure. Norwegian University.
- 686 Pelayo, F., Skafte, A., Aenlle, M. L. and Brincker, R. (2015). Modal Analysis Based
687 Stress Estimation for Structural Elements Subjected to Operational Dynamic
688 Loadings. Exp. Mech., 55(9), 1791–1802. <https://doi.org/10.1007/s11340-015-0073-6>
689
- 690 Rezaei, R. (2017). Fatigue Sensitivity of Monopile-supported Offshore Wind Turbines.
691 University College London.
- 692 Rezaei, R., Duffour, P. and Fromme, P. (2018). Scour influence on the fatigue life of
693 operational monopile-supported offshore wind turbines. Wind Energy, 21(9),
694 683–696. <https://doi.org/10.1002/we.2187>
- 695 Rudolph, D., Bos, K. J., Luijendijk, A. P. and Rietema, K. (2016). Scour around off-
696 shore structures-analysis of field measurements.
- 697 Shahmohammadi, A. and Shabakhty, N. (2020). Pile Apparent Fixity Length Estima-
698 tion for the Jacket-type Offshore Wind Turbines under Lateral Loads Applica-
699 ble to Fatigue Analysis. Int. J. Coast. Offshore Eng., 3(4), 25–33.
700 <https://doi.org/10.29252/ijcoe.3.4.25>
- 701 Shirzadeh, R., Devriendt, C., Bidakhvidi, M. A. and Guillaume, P. (2013). Experi-
702 mental and computational damping estimation of an offshore wind turbine on a
703 monopile foundation. J. Wind Eng. Ind. Aerodyn., 120, 96–106.
704 <https://doi.org/10.1016/j.jweia.2013.07.004>
- 705 Song, J. and Achmus, M. (2023). Cyclic overlay model of p – y curves for laterally
706 loaded monopiles in cohesionless soil. Wind Energy Sci., 8(3), 327–339.
707 <https://doi.org/10.5194/wes-8-327-2023>
- 708 Sørensen, P. H. S. and Ibsen, L. B. (2013). Assessment of foundation design for off-
709 shore monopiles unprotected against scour. Ocean Eng., 63, 17–25.
- 710 Stieng, L. E. S. and Muskulus, M. (2020). Reliability-based design optimization of off-
711 shore wind turbine support structures using analytical sensitivities and factor-
712 ized uncertainty modeling. Wind Energy Sci., 5(1), 171–198.
713 <https://doi.org/10.5194/wes-5-171-2020>
- 714 Tang, Z., Melville, B., Shamseldin, A., Guan, D., Singhal, N. and Yao, Z. (2023). Ex-
715 perimental study of collar protection for local scour reduction around offshore
716 wind turbine monopile foundations. Coast. Eng., 183, 104324.
717 <https://doi.org/10.1016/j.coastaleng.2023.104324>

- 718 van der Tempel, J. (2006). Design of support structures for offshore wind turbines.
719 Technische Universiteit Delft.
- 720 Velarde, J., Kramhøft, C., Sørensen, J. D. and Zorzi, G. (2020). Fatigue reliability of
721 large monopiles for offshore wind turbines. *Int. J. Fatigue*, 134, 105487.
722 <https://doi.org/10.1016/j.ijfatigue.2020.105487>
- 723 Wang, G., Xu, S., Zhang, Q. and Zhang, J. (2023). An experimental study of the local
724 scour protection methods around the monopile foundation of offshore wind tur-
725 bines. *Ocean Eng.*, 273, 113957.
726 <https://doi.org/10.1016/j.oceaneng.2023.113957>
- 727 Wang, L., Zhou, W., Guo, Z. and Rui, S. (2020). Frequency change and accumulated
728 inclination of offshore wind turbine jacket structure with piles in sand under
729 cyclic loadings. *Ocean Eng.*, 217, 108045.
730 <https://doi.org/10.1016/j.oceaneng.2020.108045>
- 731 Wang, X., Zeng, X., Li, X. and Li, J. (2019). Investigation on offshore wind turbine
732 with an innovative hybrid monopile foundation: An experimental based study.
733 *Renew. Energy*, 132, 129–141. <https://doi.org/10.1016/j.renene.2018.07.127>
- 734 Zdravković, L., Taborda, D., Potts, D., Jardine, R., Sideri, M., Schroeder, F., Byrne, B.,
735 McAdam, R., Burd, H., Houlsby, G., et al. (2015). Numerical modelling of large
736 diameter piles under lateral loading for offshore wind applications. *Front. Off-
737 shore Geotech. III*, 759–764.
- 738 Zhang, F., Chen, X., Feng, T., Wang, Y., Liu, X. and Liu, X. (2022). Experimental
739 study of grouting protection against local scouring of monopile foundations for
740 offshore wind turbines. *Ocean Eng.*, 258, 111798.
741 <https://doi.org/10.1016/j.oceaneng.2022.111798>
- 742 Zhang, F., Chen, X., Yan, J. and Gao, X. (2023). Countermeasures for local scour
743 around offshore wind turbine monopile foundations: A review. *Appl. Ocean
744 Res.*, 141, 103764. <https://doi.org/10.1016/j.apor.2023.103764>
- 745 Zhang, H., Liang, F. and Zheng, H. (2021). Dynamic impedance of monopiles for off-
746 shore wind turbines considering scour-hole dimensions. *Appl. Ocean Res.*, 107,
747 102493. <https://doi.org/10.1016/j.apor.2020.102493>
- 748 Zhang, R., Zhao, Z. and Dai, K. (2019). Seismic response mitigation of a wind turbine
749 tower using a tuned parallel inerter mass system. *Eng. Struct.*, 180, 29–39.
750 <https://doi.org/10.1016/j.engstruct.2018.11.020>
- 751
752